Coding of Non-Linear White-Light Luminescence from Gold-Silicon Structures for Physically Unclonable Security Labels

Ekaterina Ponkratova, Eduard Ageev, Peter Trifonov, Pavel Kustov, Martin Sandomirskii, Mikhail Zhukov, Artem Larin, Ivan Mukhin, Thierry Belmonte, Alexandre Nominé, Stéphanie Bruyère, and Dmitry Zuev*

Luminescent security labels are effective platforms for protection of consumer goods from counterfeiting. However, the lifetimes of such security approaches are limited due to narrow-band photoluminescent features of the label elements, which can be used for the protection technology disclosure. In this paper, a novel concept for the application of non-linear white-light luminescence from hybrid metal–semiconductor structures fabricated by direct femtosecond laser writing for the creation of physically unclonable security labels is proposed. A close connection is demonstrated between the internal composition of hybrid structures, which is controlled at the fabrication stage, and their non-linear optical signals. It is shown that the application of decorrelation procedure based on discrete cosine transform and polar codes for label coding can overcome the problem of the white-light photoluminescent spectra correlation. The proposed fabrication approach and coding strategy allows reaching a high degree of device uniqueness (up to 99%), bit uniformity (close to 0.5), and encoding capacity up to 1.25×10^{437} in a single label element. The results demonstrate that the barriers for the application of white-light luminescent nano-objects for the creation of physically unclonable labels are removed.

1. Introduction

Fake consumer goods cause huge financial losses in industry and affect many areas of life, posing a threat to individuals, corporations, and society as a whole.[1,2] A striking example is counterfeiting of medicine. According to the World Health Organization, over 10% medicines in low and middle-income countries are falsified.[3] Counterfeit medicine is extremely dangerous, considering that substandard and falsified medicines can even cause lethal cases. Such data clearly illustrate that counterfeit is a serious threat to humanity. Among the frequently used methods of protecting goods from forgery are various protective labels: RFID tags,[4] barcodes,[5] holograms,[6] watermarks,[7] protective inks,[8] and others. Usually, a combination of several methods is used to increase the level of protection. Despite this fact, such a protection is not absolute due to its deterministic encoding and corresponding decoding mechanisms. The safety of these methods mainly depends on technical barriers and limited access to equipment and materials. Therefore, the development of novel approaches for the next-generation anti-counterfeiting systems is a challenge for science and industry.

Security labels based on physical unclonable functions (PUF) are a practical solution to this problem.[9] This term refers to a physical object with unique properties obtained with random or non-deterministic processes, which, in turn, makes the possibility of reproducing it vanishingly small. To date, various designs of PUF labels were proposed, based on intrinsic surface topology of the product,[10,11] randomly distributed nanostructures,[12–16] unique pattern distribution,[17–19] and so on.

Creation of security labels whose uniqueness is based on optical characteristics such as speckle pattern,[20] light polarization,[21] Raman scattering,[22] reflectance,[23,24] and photoluminescence (PL)[25,26] is very promising, as optical reading is a non-contact, fast, and relatively convenient method that provides high encoding performance using multiple spectral functions.

Among the numerous technologies elaborated for the security labels creation, luminescent nanosystems attract particular interest.[27,28] Currently, anti-counterfeiting systems based on up- and down-conversion luminescent materials are widely

E. Ponkratova, E. Ageev, P. Trifonov, P. Kustov,
M. Sandomirskii, M. Zhukov, A. Larin, I. Mukhin,
A. Nominé, D. Zuev
School of Physics and Engineering
Faculty of Secure Information Technologies
ITMO University
Kronverksky Pr. 49, bldg. A, St. Petersburg 197101, Russia
E-mail: d.zuev@metalab.ifmo.ru

M. Zhukov
Laboratory of Scanning Probe Microscopy and Spectroscopy
Institute for Analytical Instrumentation RAS
St. Petersburg 198095, Russia

I. Mukhin
Center for Nanotechnologies
Alferov University
Khlopina str. 8, St. Petersburg 194021, Russia

I. Mukhin
SCAMT Institute, ITMO University
Khlopina str. 8, St. Petersburg 197101, Russia

T. Belmonte, A. Nominé, S. Bruyère
Institut Jean Lamour, CNRS – Université de Lorraine
UMR CNRS 7198, Nancy F-54011, France

The ORCID identification number(s) for the author(s) of this article can be found under https://doi.org/10.1002/adfm.202205859.
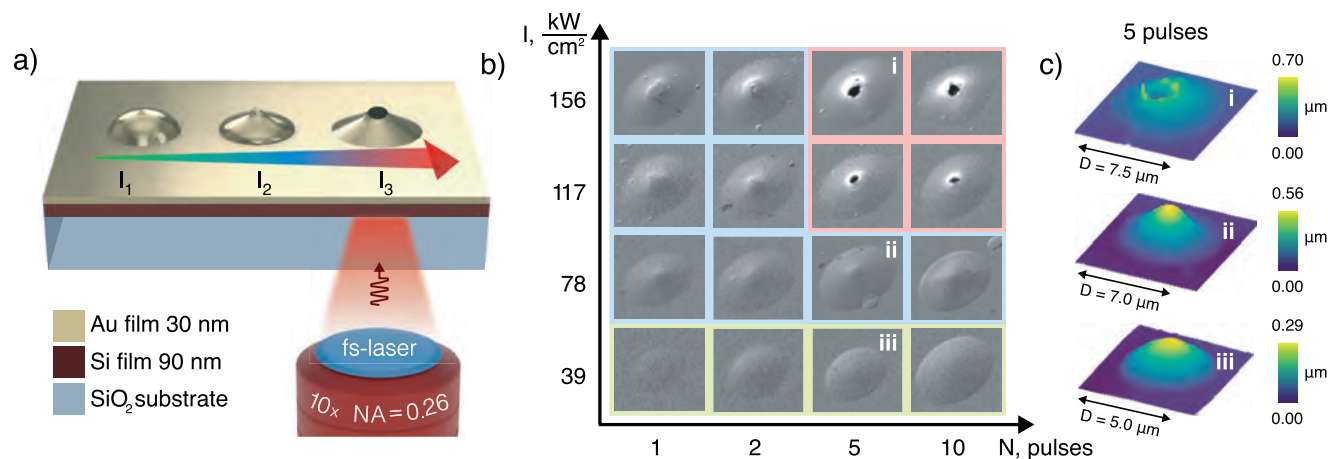
Figure 1. Hybrid metal–semiconductor structures. a) Fabrication scheme; b) SEM images of the hybrid structures (the observation angle is 45°); c) AFM images of the three typical geometries.

studied and even integrated in some industrial applications, for example, in banknotes.[29] But with time, simple luminescence-based security technologies are inevitably repeated and cannot meet the current protective criteria. The next steps in the evolution of luminescent security labels are the application of new luminescent materials with high luminescence stability and intensity, development of non-standard designs of luminescent security labels and others. The common demand to all new types of luminescent labels is the combination of high security level and low-cost and simple fabrication.[30]

From this point of view, laser-assisted techniques providing wide fabrication opportunities are very attractive.[31,32] Indeed, precise control over the laser beam parameters and irradiation mode of the sample surface provide wide opportunities for the realization of security labels with various designs. For example, lasers have already proven to be effective in the fabrication of anti-counterfeiting based on colored protection patterns on a metal surface.[33,34] Currently, in the laser-assisted fabrication of security labels, narrow-band luminescent patterns are created,[35–37] based on the narrow-band PL or combination of different luminescent systems.

This is a conventional approach to luminescent security label design,[28,30] effective for registration and decoding, but vulnerable to label hacking and duplication. Therefore, other approaches to the luminescent labels' design should be considered, such as tuning of luminescent spectra under external stimuli,[38] lifetime encoding,[39] and broadband PL.[40] The latter can be considered as a promising approach for the creation of luminescent security labels based on nano-objects with white-light PL. In this case, application of a wide PL spectral range for the label encoding/authentication eliminates the problems related to the reduced security lifetime of narrow-band PL technologies. However, this feature has difficulties related to the similarity and correlation of white-light luminescent spectra in coding/authentication procedures, which hinders the use of such labels and their fabrication methods.

In this paper, we demonstrate the application of single-step laser fabrication method for the creation of three types of structures with different non-linear responses after irradiation of Au/Si thin film surface. To understand the origin

of the non-linear response behavior, we studied the internal microstructure of the fabricated systems with high-resolution transmission electron microscopy (HRTEM) technique. We demonstrate that the difference in the non-linear behavior and the white-light luminescent signal of the fabricated systems can be used for the creation of multilevel security labels.

2. Results and Discussion

2.1. Fabrication and Characterization

A distinctive feature of laser-assisted nanofabrication is the capability to obtain objects with absolutely different geometries from the same sample by reconfiguring the laser irradiation parameters. In this work, we fabricated hybrid metal–semiconductor structures with three different geometries. As an initial sample, we used a bi-layered Au/Si film with thicknesses of 30 and 90 nm, respectively, on a glass substrate. We created the structures by the irradiation of the film surface in the transmittance geometry (**Figure 1**a).

The fs-laser pulses with a wavelength of 1050 ± 3 nm were tightly focused on the film surface in the spot with diameter $D \approx 4 \, \mu m$. The structures were produced by moving the sample in two perpendicular directions in the sample surface plane and varying the average power density (I) and the number of laser pulses incident at one point (N). Figure 1b shows the scanning electron microscopy (SEM) images of the produced structures, which were tilted by 45° with respect to the normal. This figure illustrates that different combinations of variable parameters lead to the formation of structures with different shapes and sizes. For instance, irradiation of the sample with $I = 39 \, kW \, cm^{-2}$ leads to the formation of parabolic structures, whose diameters grow with an increase of the number of incident pulses. Irradiation of the sample with $I = 78 \, kW \, cm^{-2}$ leads to the formation of conical structures, and the same dependence of their diameters on N is the same as in the previous case. Similar structures were created under irradiation with $I = 117$ and $156 \, kW \, cm^{-2}$ in single and double-pulse regimes, but the peaks in the center of the produced structures are more
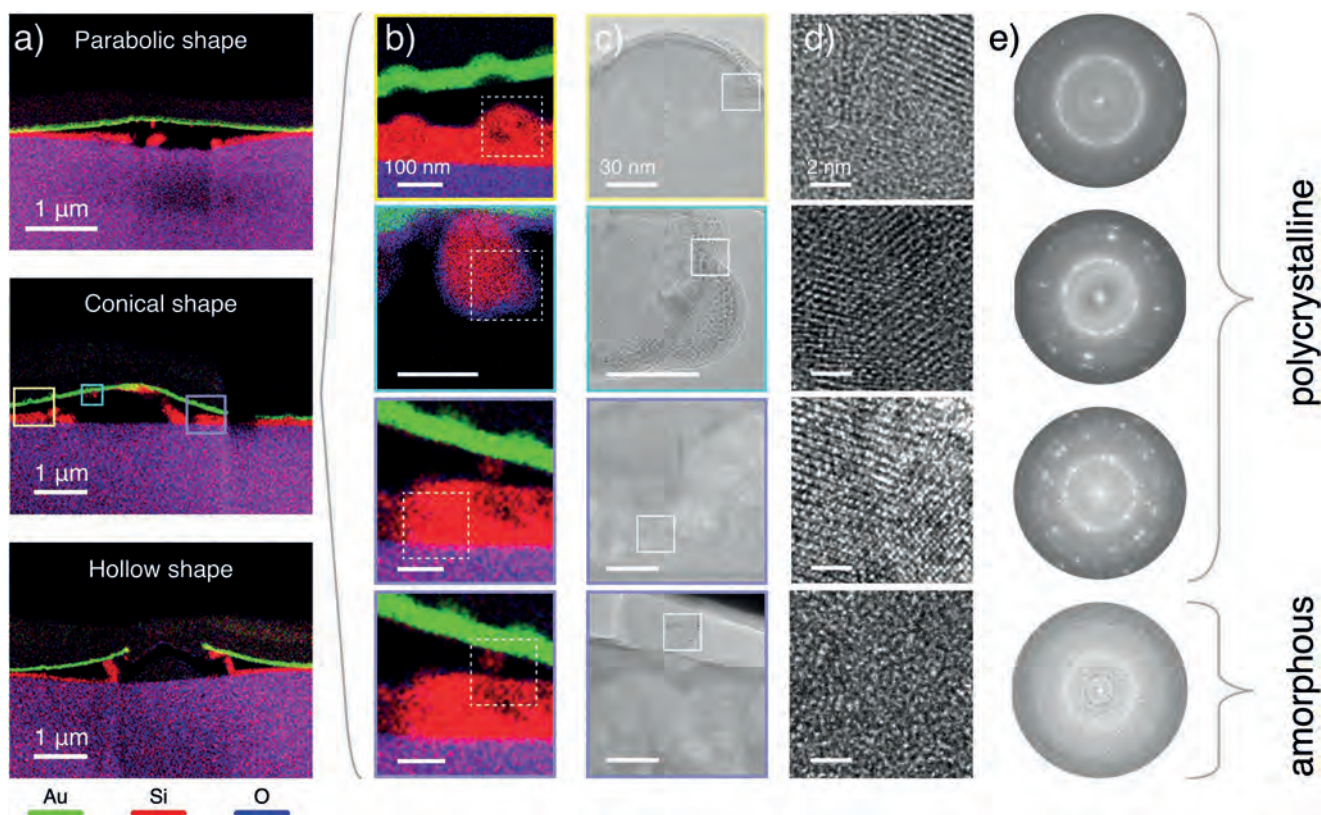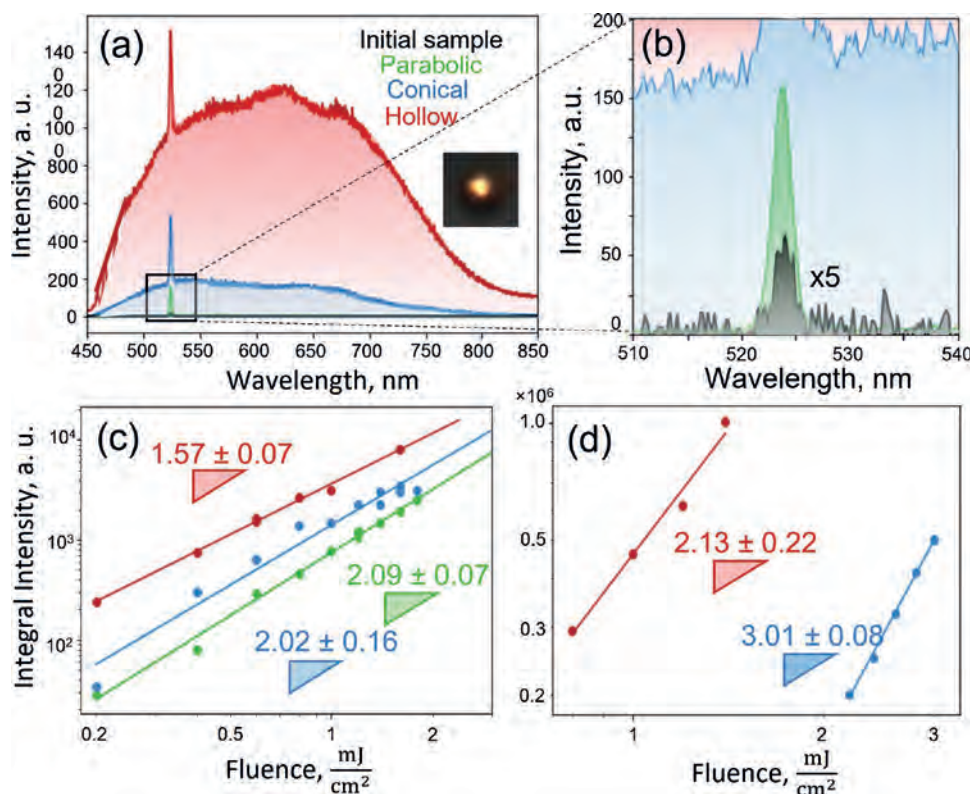
Figure 2. Analysis of the geometry and inner composition of the hybrid systems. a) STEM-EDS maps of structures' cross sections, which show films bending under laser irradiation; b) magnified STEM-EDS maps areas of conical structure profile and c) TEM, d) HRTEM, and e) FFT HRTEM analysis of these areas.

pronounced in these regimes. Holes with different diameters (1–2 µm) instead of sharp peaks were created under irradiation with average power densities of 117 and 156 kW cm^{-2} in the 5 and 10-pulse regimes. The proposed approach demonstrates high repeatability for the gold–silicon structures fabrication and enables the creation of arrays consisting of such nanostructures (see Section S1, Supporting Information). To provide a detailed analysis of obtained hybrid systems with atomic resolution, transmission electron microscopy (TEM) was applied. To see the elemental distribution inside the considered structure, the energy-dispersive X-ray spectroscopy (EDS) mapping was also provided in the scanning mode (scanning transmission electron microscopy [STEM]), in parallel with the TEM analysis. **Figure 2**a shows the EDS analysis of parabolic, conical, and hollow structures.

This figure shows that for all structures, both gold (green color) and silicon (red color) films are elongated perpendicular to the surface. Further, due to low plasticity, the silicon film has a sharp bending, while the plastic gold film has a smooth bending profile. In addition, a lack of silicon in the central part of the structure is observed in the EDS maps. This lack of material can be explained by its possible loss during the sample preparation for the TEM measurements. For a more detailed analysis of the hybrid systems, we chose several parts of the conical structure, marked with boxes in Figure 2a. These areas are and magnified in Figure 2b, and further investigated these areas with TEM microscopy. Figure 2c,d shows

the corresponding TEM and high-resolution TEM (HRTEM) images for the same areas. Fast Fourier transform (FFT) analysis of these HRTEM areas are presented in Figure 2e. From FFT HRTEM analysis, we can conclude that on the edges of the structure, the silicon is in amorphous phase. Closer to the central part, the film consists of differently oriented grains of Si (cubic structure Fd-3m). As crystalline materials contain an ordered arrangement of atoms, the electrons incident on these atoms can be diffracted only at specific angles. Electrons diffracted at these directions are seen as spots on the image. In turn, the gold film (depicted with green on the EDS maps) is completely crystallized on the entire lamella of the focused ion beam (i.e., in the laser-irradiated zone). For parabolic and hollow structures, similar behavior for gold and silicon films is observed, and we do not present their analysis for this reason.

These studies reveal the processes leading to the hybrid systems formation from the two-layered gold–silicon thin films. The shape of such a hybrid nanosystem is mainly determined by the modification of the gold layer. The changes in the Au film profile can be described by the Marangoni effect (elasto-plastic flows model).[41,42] According to this model, when an incident Gaussian pulse irradiates the film surface, after several picoseconds of electron-ion temperature relaxation, the gold film is heated with radial temperature gradients oriented from the center to the edges of the irradiated area. These temperature gradients lead to thermal stresses in the film, which, in turn increase the momentum along the normal to the sample

**ADVANCED
SCIENCE NEWS**

www.advancedsciencenews.com

**ADVANCED
FUNCTIONAL
MATERIALS**

www.afm-journal.de

Figure 3. Nonlinear optical properties of hybrid structures; a) PL signal of the initial film (black), and parabolic (green), conical (blue), and hollow (red) structures; b) magnified areas from (a); Dependence of integral values of c) SHG and d) broadband PL signals on the pump power. Insets on figure red (a): photos of shining structures under fs-pulses pumping.

surface. These bending strains lead to the formation of a parabolic structure. For increased power density, a conical structure (a parabolic system with an additionally elongated central part) is formed. At such and lower power densities the film is heated to the values when stretching can be stopped by surface tension. A hole forming in the central part can be described by dewetting processes in the melted part of the film with an additional increase of the power density.

The thin Si layer additionally affects the hybrid system formation. The Si layer starts to crystallize at power densities lower than the one needed for parabolic structure creation. In this case, silicon crystallites begin to grow in the film volume, with no mixing with the Au layer. This scenario is additionally proved by the observed second harmonic generation (SHG) with no white-light (WL) signal (see **Figure 3**). As the power density increases and conical and hollow structures form, the volume of crystallites in the Si film starts to grow, and Au–Si mix mutually. As a result, the white-light signal is observed in the photoluminescence (PL) spectra in addition to the SHG signal. In this case, hydrodynamic interaction between the Si layer and silica substrate provides a momentum detaching the central part of Si film, which is mostly crystallized. This effect can be seen on the HRTEM images of these structures in the central part (Figure 2d).

The origin of silicon crystallinity variation along the structure is related with inhomogeneous distribution of laser energy along the laser spot area. Indeed, in case of Si films crystallization by a single laser spot the formation of zones with different amounts of a-Si and p-Si was observed in the spot due to the Gaussian distribution of the laser intensity.[43] The observed crystallinity variation has a direct impact on PL of the structures due to Auger recombination of non-thermalized hot charges excited by multiphoton absorption,[44–46] which depends on the phase of the semiconductor and its crystallinity. Such an effect was demonstrated in hybrid gold–silicon nanoparticles, when the growth of Si crystallinity has a favorable effect on the photoluminescence of Au/Si nanostructure.[47]

2.2. Nonlinear Optical Properties Studies

The observed internal composition of the parabolic, conical, and hollow structures are directly connected to their non-linear optical properties. To analyze the nonlinear optical properties of the structures, we used the same femtosecond laser system, with repetition rate changed to 80 MHz. The collected optical signals from structures obtained under laser pumping with a fluence of 2 mJ cm^{-2} are summarized in Figure 3a and normalized spectra are demonstrated in Figure S3, Supporting Information (see Section S2, Supporting Information).

The excitation of structures by NIR-fs-radiation is accompanied, for the most part, by two nonlinear processes: SHG and multi-photon-induced white light PL of the silicon. SHG is a special case of the sum-frequency generation, where two equal pump photons λ_{exc} are converted into one at double-pump-frequency $\lambda_{SHG} = \lambda_{exc}/2$, where full-width at half maximum

**ADVANCED
SCIENCE NEWS**

www.advancedsciencenews.com

**ADVANCED
FUNCTIONAL
MATERIALS**

www.afm-journal.de

(FWHM) of SHG determined as $FWHM_{SHG} = FWHM_{exc}/2^{1.5}$.[48] With respect to this definition, the nature of the narrow peak in the emission spectrum was determined. The basis of silicon PL is the Auger recombination of non-thermalized multi-photon-induced hot-carriers.[44–46] The properties of PL radiation in such a process are determined by the interaction of the electronic and phonon subsystems. Therefore, the silicon dispersion of electrons and phonons is very important in this matter.

The signal from the initial sample (two-layered Au/Si thin film) is shown with black curve on Figure 3b. As one can see, the non-radiated sample emits only a weak SHG signal at the wavelength of 525 nm under fs-laser pumping. The nature of this peak might be related to symmetry breaking due to surface defects.[49] For the parabolic structure, the SHG signal was enhanced tenfold compared to the initial film (green curve). This enhancement can be explained by local breaking of inversion symmetry[50] due to the net of interfaces separating different crystalline Si grains, produced by laser irradiation. For conical structure, the SHG signal was enhanced even higher (blue curve), 20-fold compared to the initial sample. However, in parallel with SHG signal, a broadband PL signal was observed in the almost entire visible range. If we assume the relationship between the generated PL and surface plasmonic polariton (SPP), we can conclude that the SPP radiation is emitted at the point of gold thinning (the top of the conical structure, see Figure 2).

The same features of the optical signal were noticed for hollow structure (red curve), but the intensity of the signal was several times higher. In this case it can be seen even with a naked eye through the micro-objective on the CCD camera as a white-light point (see the inset on Figure 3a). For such hollow structures the SPP emission occurs more easily than in the case of a conical structure due to the presence of a hole in the gold film. Therefore the bright PL emission is observed precisely at the point of break of the Au film.

To describe the non-linear response behavior, the intensity dependencies over pump power were performed for all three structure shapes. Figure 3b shows the spectra of the SHG signal for the structure series. The integral intensity of SHG was calculated as follows. Two edge points at 520 and 527 nm, which correspond to the transition between SHG and WL signals on the spectra, were reset to zero by baseline, and integral values under the obtained curves were calculated. These integral values corresponding to specific pump powers are marked by dots in Figure 3c. Solid lines represent polynomial fit as $I_{SHG} = f(P_{exc}) \sim P_{exc}^n$, where n indicates polynomial order and acts as line slope in log–log graph representation. The slopes for the SHG signal are close to 2.09 ± 0.07, 2.02 ± 0.16, 1.57 ± 0.07 for parabolic, conical, and hollow shape structures, respectively. Basically, SHG intensity has a quadratic dependence on the pump power: $I_{SHG} = |\chi^{(2)}|^2 P_{exc}^2$, where $\chi^{(2)} \neq f(P_{exc})$ is second-order nonlinear susceptibility. Any deviation from the quadratic dependence leads to the conclusion that the second-order nonlinear susceptibility depends on the pump power $\chi^{(2)} = f(P_{exc})$. Just in the case of hollow shape structures, the SHG signal begins to deviate from the quadratic dependence and exhibits a bright PL signal. This behavior of SHG is similar to the behavior shown early,[51] where the physics of the process is assumed to be the mechanism of energy exchange between SHG and PL at a high electron–hole plasma density.

The same dependencies were plotted for broadband PL signal. Integral intensities for this case were calculated by integrating over the considered wavelength range, subtracting the integral value of the SHG signal. The results of these calculations are shown in Figure 3d. The obtained slopes are 3.01 ± 0.08 and 2.13 ± 0.22 for the conical and the hollow structures, respectively. Based on these data, we can conclude that the two- and three-photon absorption processes make the main contribution to the white-light PL signals. It is widely known that the efficiency of light absorption by silicon is low due to its indirect band gap. In our case, hot carriers injection from gold to silicon by two- and three-photon absorption processes can be the mechanism behind the absorption efficiency enhancement.[52] We assume that a combination of radiative, Auger, and defect-assisted relaxation processes further contributes to this enhancement, leading to the emission of photons with different energies and formation of broadband PL signal. The difference in slopes can be due to different conditions of electron–hole plasma excitation for different shape types of structures. These assumptions demonstrate a potential model of white-light generation.
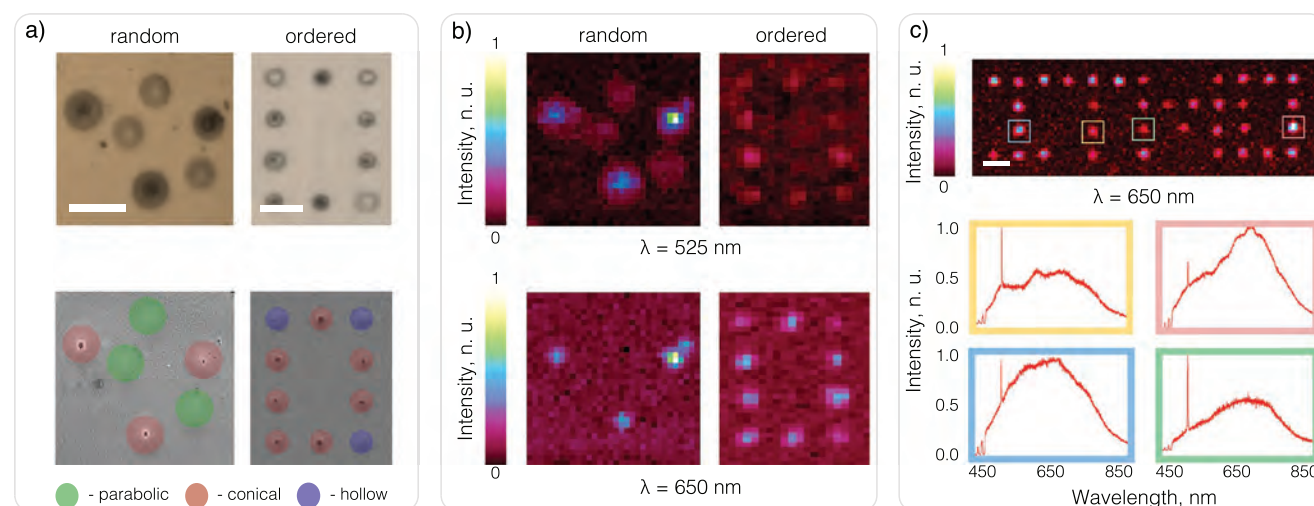
Thus, we have developed a fabrication method of hybrid metal–semiconductor structures, achieving with different non-linear responses from the same bi-layered Au–Si thin film. The control over the internal microstructure of the hybrid systems, which modifies the non-linear response, is provided by simple variation of the laser beam parameters such as average power density and number of incident pulses. Importantly, even for hybrid structures of the same type (conical or hollow), the white-light luminescent spectra are inherently unique due to the accidental morphology deviations of the structures' geometry. This deviation can be explained by the stochastic features of fabrication processed and surface inhomogeneity of the initial film.

To study the stability of produced nanostructures the additional measurements of their PL were done. The studies demonstrate that PL spectra are stable during 20 min of continuous measurements, at heat up to 49 °C, or over-one-year storage in the lab environment (see Section S3, Supporting Information).

These features, combined with the ability to easily change the type of structure and mutual spatial positions of several structures, opens up good prospects for the use of laser-induced hybrid structures for security labels.

2.3. Creation of Security Label Patterns

Security labels are usually made of building blocks arranged on a surface in a special pattern, which is revealed under external stimuli. Thus, luminescent security labels are illuminated at a certain wavelength. In our case, due to flexibility of laser-assisted fabrication process, various types of hybrid nanosystems can be distributed over the film area, forming a selected pattern or randomly. To demonstrate this opportunity, we recorded two types of patterns (see **Figure 4**a). The first one consists of randomly distributed parabolic and hollow structures. The second one is a combination of conical and hollow structures forming a rectangle. The top images in Figure 4a

**ADVANCED
SCIENCE NEWS**

www.advancedsciencenews.com

**ADVANCED
FUNCTIONAL
MATERIALS**

www.afm-journal.de

Figure 4. Femtosecond laser fabrication of Au/Si structures for the creation of unclonable security labels. a) Spatial location and combination of different types of structures; b) maps of the SHG signal (top) and white-light luminescent signal at a wavelength of 650 nm (bottom) for the areas shown in figure (a); c) Demonstration of the PUF label recording. Scale bars correspond to 10 μm in (a,c).

show the optical image of these labels, and the bottom ones demonstrate SEM microphotographs.

Under a small optical magnification (no more than 10×), no clear differences are observed between structures of the same type. However, a more precise equipment for visualization, for example, an objective with a high M and NA, or a SEM system, reveals a slight difference for the hollow structures (see Figure 4a). In this case, the optical imaging was performed with an objective with parameters of M = 50×, NA = 0.42.

The non-linear optical response of the hybrid structures, calculated as the ratio between the intensities of the SHG signal and white-light luminescence, is directly connected to the structure type. To demonstrate this, we performed nonlinear optical signal mapping of the structure patterns, illustrated in Figure 4b. Top images in Figure 4b show the signal observed at a wavelength of 525 nm (SHG signal), and the bottom images show the signal at a wavelength of 650 nm (a randomly selected wavelength from the broadband PL signal). Comparing these maps at different wavelengths, we clearly see that the nonlinear signals from hollow structures are more intense than those of for parabolic and conical structures. Additionally, the parabolic structures do not demonstrate white-light signals and are therefore hidden on the luminescent map made at a wavelength of 650 nm. Thus, the features of nonlinear signals of different types of structures can be used for creating protection levels authenticated only under deep laboratory examination of the label.
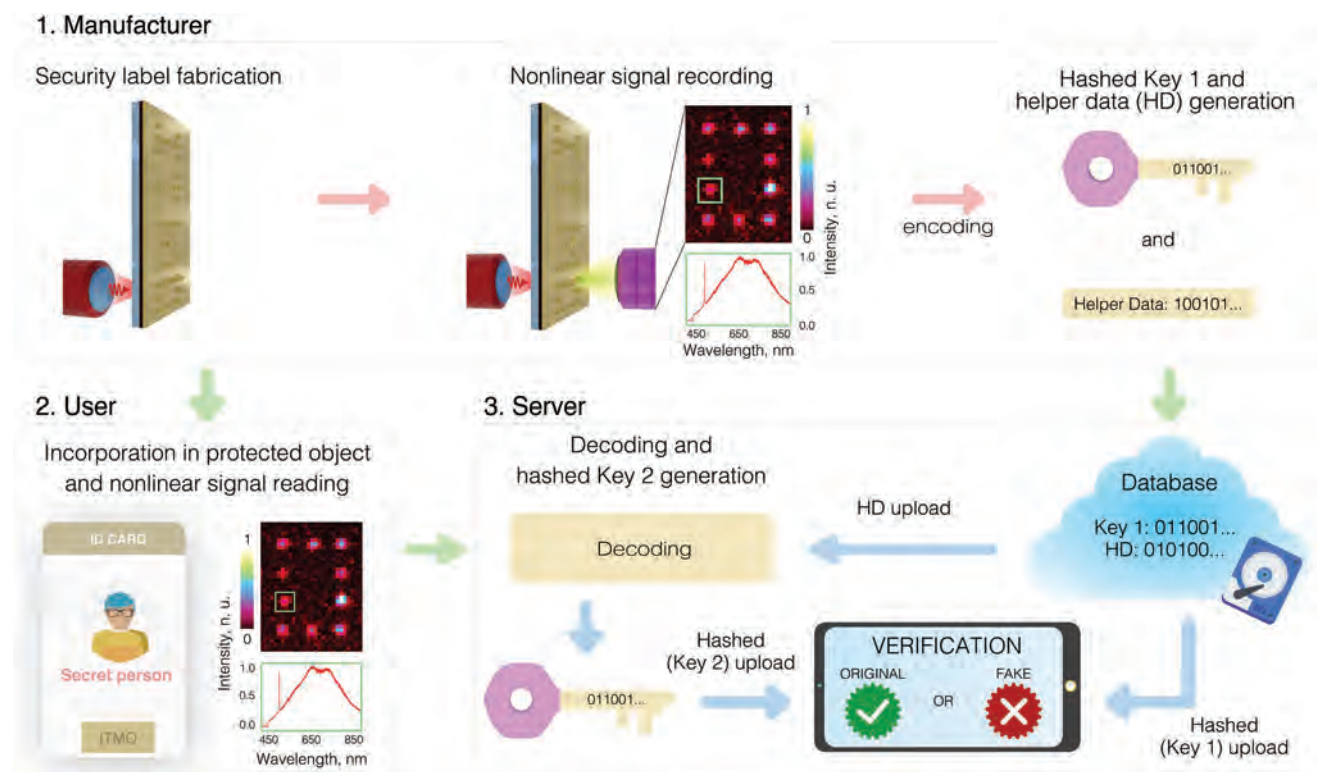
In should be noted that the shape of the white-light PL signals for conical and hollow structures have deviations, unique for each structure. This feature can be used to create physically unclonable security labels. Such labels are based on the properties of stochastically distributed objects, for example, luminescent signal[53–55] or Raman response.[22,56] In our case, the opportunity to fabricate hybrid structures with a predetermined pattern allows the creation of luminescent labels combining the benefits of conventional labels with a specific

arrangement of elements with physically unclonable properties. Indeed, even with the spatial arrangement of structures of the same type that create some logo, their spectral form of luminescent white light signals is stochastic.

To demonstrate such a design, we have fabricated a logo consisting of the hollow structures (Figure 4c). For the logo authentication, several structures were chosen, indicated by color boxes in the map. Their nonlinear signals in the range from 450 to 850 nm are shown below the map in the frames of corresponding colors. The signal from one structure consists from pixels, and their number depends on the scanning resolution. For the white-light spectrum determination, the signals from the pixels of a certain structure are averaged and normalized to the signal maximum (see Section S4, Supporting Information). Although all the considered structures look similar in the map, the shape and intensity of optical nonlinear signals for each structure differ from each other. Thus, the fingerprints of the label elements include the type of structure, its relative position, type of non-linear signal, and white-light PL spectral signature.

Therefore the demonstrated systems can be applied for realization of the multilevel security concept. Such a concept includes three security levels based on geometry and nonlinear optical properties features of fabricated structures. Here we use a spatial location and combination of different types of structures as the first level. At the second level a dependence of nonlinear optical signal intensity on type of the structure is used, while the third level is based on the uniqueness of spectra of each structure.

To understand the reproducibility of a nonlinear optical signal when reading the same point, a nonlinear signal map was recorded for three types of structures (see Section S1, Supporting Information). It can be found (Figure S2b, Supporting Information), that the obtained spectra for different readings are almost identical. Therefore, the mapping of a nonlinear signal provides a high repeatability of fluorescence spectrum measurement for each type of structure.

**ADVANCED
SCIENCE NEWS**

www.advancedsciencenews.com

**ADVANCED
FUNCTIONAL
MATERIALS**

www.afm-journal.de

Figure 5. Potential scheme of object protection by the security label based on Au/Si structures. First, a manufacturer creates a security label and records its nonlinear signal map. The spectra averaged over each element of the label are decorrelated via discrete cosine transform and converted to the Key 1 and helper data (HD) by polar codes. The obtained Key 1 is hashed and uploaded with HD to a database. At the next step, the user reads the label incorporated into a protected object.

2.4. Enrollment and Authentication of PUF Label

Figure 5 illustrates the enrollment and authentication scheme of the proposed PUF label. First, a manufacturer chooses the desired configuration of a security label (the type and mutual position of laser-induced structures) and produces it by previously discussed laser fabrication method. Further, the manufacturer records a nonlinear signal map of the fabricated label. Then, the non-linear spectra from each element of the label are averaged over its entire area and normalized, and the noise is removed.

Generally speaking, the non-linear PL spectra are quite close in terms of the SHG signal peak position and general spectral shape of the white-light signal. In fact, intensity/coordinate points describing the shape of the PL signal are correlated. However, each individual spectrum is unique, and to take full advantage of this uniqueness for PUF label encoding, signal points are decorrelated through a discrete cosine transformation (see Section S5.3, Supporting Information).

Next, the decorrelated data is encoded to obtain the PUF key. The required encoding method should both have a low false-positive rate and be resistant to noise that occurs when reading the label. Thus, the encoding protocol should be developed carefully.

Here we propose a key generation scheme based on multilevel polar codes.[57,58] Variations of this approach are widely used in cryptography and are dedicated to PUF-based secret generation for device authentication.[59–61] Essentially, polar code is an error-correcting code designed to control errors when transmitting data over noisy channels. And to apply this encoding technique for our case, we use polar codes as component codes in multilevel encoding of decorrelated data obtained after discrete cosine transformation (see Section S5.1 and S5.2, Supporting Information). At the enrollment stage after decorrelation and normalization of the data (see Section S5.3, Supporting Information) we get the set X_j (**Figure 6**). Then, we apply a multistage successive cancellation decoder for a multilevel polar code to this set. As a result of this procedure we obtain the unique Key 1 and helper data (HD) which will be needed later as a hint at the authentication stage. Then, Key 1 is hashed and uploaded with HD to a database by the manufacturer.

Further, a person checking the label authenticity (user) reads the label. We assume that this label is supplied with a digital identifier $\mathcal{I}$. A distorted spectrum of the label is obtained, decorrelated, and normalized using the same parameters at the enrollment stage. Then, the helper data corresponding to $\mathcal{I}$ is requested from the database. Multistage successive cancellation decoder is applied to transformed points of the measured spectrum, where part of the bits is determined using the received HD. The decoder recovers the remaining bits, that is, it produces an estimate of the secret—Key 2. This estimate is hashed and compared with the hashed Key 1 stored in the database. For more information see Section S5.4, Supporting Information.
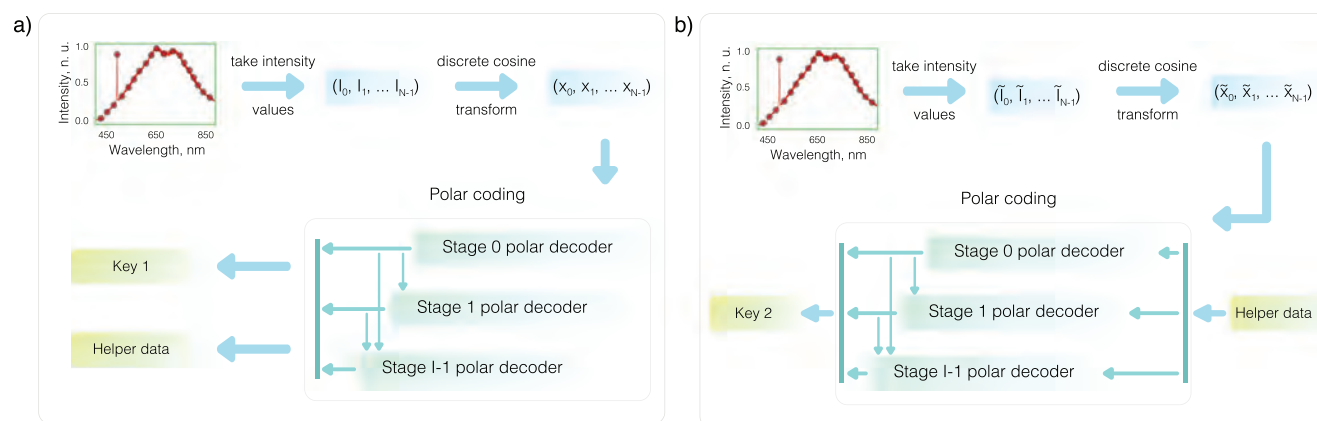
Figure 6. The stages of the measured spectra conversion into a unique key. a) Key and HD generation by the manufacturer; b) Key obtaining with the use of HD requested by the user.

If the hashed keys coincide, the label can be defined as the original one. The results are sent to the user, confirming or rejecting rejection of the label originality. As a result, due to the uniqueness of each fabricated label, the user can be confident that the verification results are reliable.

One of the advantages of our method is that the keys obtained from different readings of the same label are completely the same and the probability of error with the parameters we used is 2%. This value can be significantly reduced, for example by reading the label several times. Also, at the enrollment stage, when generating keys and helper data, the number of bits written to the helper data can be increased. This will cut the length of the key (and hence the capacity of the label), but it will reduce the likelihood of error as well.

For comparison, we have calculated intra-chip Hamming distance for the measured spectras after the stage of their decorrelation but before applying multilevel polar codes (see Section S6 and Table S1, Supporting Information).As a result, we report a value of bit error rate from 4.3% to 22% for different bits of data showing a high effect of noise and confirming the need for a competent encoding method. This only justifies the use of multilevel polar codes in our scenario.

The proposed security labels with different numbers of separate elements have inherently non-repeatable luminescent characteristics. The protection of such labels is mainly determined by the uniqueness of their individual elements. To demonstrate the originality of the label elements, their main individual parameters such as the secret key length s, encoding capacity (EC), bit uniformity, and device uniqueness were estimated using hollow-type structures as an example. The results of the parameters' estimation yield more than a hundred white-light luminescent spectra, presented in **Table 1**. The details of the estimation are available in Section S6, Supporting Information.

From the table, we can see that an increase of number of levels in multilevel polar codes - l leads to a nonlinear increase of the secret key length, s. Thus, for $l = 4$, it reaches 1452, which corresponds to EC for the parabolic structure as 2^{1452} or 1.25×10^{437}.

Such an estimation allows us to calculate EC for a logo made of n elements as EC $= (2^s)^n$. For the logo, demonstrated in Figure 4c and consisting of 35 unique points of the same type (hollow structures), EC reaches a value of $2^{1452*35}$ or 2.21×10^{15298}. This value fully satisfies the criterion for the EC of physically unclonable labels, exceeding the value of 10^{300}.[9]

Another important parameter is bit uniformity, which can be calculated by the formula (See Section S3, Supporting Information); for an ideal unclonable object, it should be close to 0.5. For hollow-type structures, this value slightly varies around this value for $n \geq 256$, where n is the number of points in the spectrum. In case of luminescent labels based on white-light luminescent building blocks, the device uniqueness is crucial due to the general similarity of the white-light luminescent spectra. In our case, the device uniqueness is more than 0.9 for $n = 128$, and for $n \geq 256$, it corresponds to the value of 0.99. Therefore, the application of the decorrelation procedure and multilevel polar codes provides high uniqueness of the proposed PUF label design.

3. Conclusions

In summary, we have shown a laser-assisted approach for the design of non-linear optical response in metal–semiconductor structures. These structures are created by the direct fs-laser

Table 1. Encoding parameters of physically unclonable hollow-shaped elements.

Number of levels l	1				2				3				4			
n	128	256	512	1024	128	256	512	1024	128	256	512	1024	128	256	512	1024
Secret key length, s	29	61	102	341	46	136	369	1114	47	153	457	1401	50	148	459	1452
Helper data size	99	195	410	683	210	375	654	933	307	577	1032	1614	333	675	1286	2201
Bit uniformity	0.54	0.50	0.49	0.50	0.53	0.50	0.50	0.50	0.53	0.50	0.50	0.50	0.52	0.50	0.49	0.50
Device uniqueness	0.91	0.99	0.99	0.99	0.94	0.99	0.99	0.99	0.94	0.99	0.99	0.99	0.99	0.99	0.99	0.99

writing on the surface of bi-layered Au/Si thin films. We demonstrate a direct connection between their inner microstructure, studied by HRTEM, and non-linear optical signals (SHG and white-light luminescence). The opportunity to control the type of hybrid nanostructures by simple variation of laser power density and number of pulses, and by their pattern, is highly promising for the creation of luminescent security labels. We show that small deviations in the geometry of hollow structures modify their inherent white-light luminescent spectra and use this feature for creation of the PUF labels. In this design, we demonstrate for the first time that a high degree of device uniqueness (up to 99%) and encoding capacity (up to 1×10^{437}) can be achieved for the label elements. This is further supported by the decorrelation procedure and polar codes applied for their PL spectra. The obtained label characteristics allow us to consider the proposed design as a good platform for the creation of security labels with physically unclonable elements. Their uniqueness is supported by the unpredictable deviations of structures' parameters. Moreover, our research provides new insights into the design of security labels based on white-light luminescence.

4. Experimental Section

Fabrication of Initial Sample: Initially red, bi-layered Au/Si films with thicknesses of 30 and 90 nm, correspondingly, were fabricated on a silica substrate. The films were deposited in two stages. First, an amorphous silicon layer was deposited on glass substrate by plasma-enhanced chemical vapor deposition from SiH_4 precursor gas. Second, a gold layer was deposited on top of the silicon layer by magnetron sputtering.

Laser-Assisted Fabrication of Hybrid Structures: The structures were fabricated on the initial sample surface with a femtosecond laser system TEMA-150 (Avesta Project) with a wavelength of 1050 nm, pulse duration of 150 fs, and repetition rate of 80 MHz. For a better control of the fabrication process, repetition rate was decreased to 1 Hz by passing the pulse through Pockels cell-based pulse picker (OG-V, Avesta project). The average output power varied from 5 to 20 mW depending on the desirable structure. The radiation with these parameters was tightly focused on Au surface in a spot size with diameter of 4 µm from substrate side by Mitutoyo M Plan Apo NIR (M = 10×, NA = 0.26) objective.

To record arrays of structures, a piezo stage (AIST Project) was applied, which moved the sample in two perpendicular directions along the sample surface.

Outer Geometry Characterization: For external geometry characterization of structures with high accuracy, both SEM and atomic force microscopy (AFM) were used. SEM measurements were performed by Inspect (Field Electron and Ion Company, FEI) system in a vacuum chamber under pressure 10^3–10^4 Pa and accelerating voltage 20 kV in secondary electrons detection mode. AFM imaging was carried out by Ntegra Aura (NT-MDT) system in semi-contact regime with passive vibration protection. Probes of HA NC series (NT-MDT) and W cathodes were used for scanning. Sample was scanned in ambient conditions.

Inner Structure Characterization: TEM and STEM observations were performed with a microscope JEOL ARM200 cold FEG with two correctors. All STEM-EDX (energy dispersive X-rays) maps were recorded using a JEOL Centurio detector (1sr). The cross-section TEM sample preparation was made by focused ion beam (FIB) in a FEI Helio Nanolab 600i SEM (scanning electron microscope). A Pt layer was previously deposited on the surface of the sample to protect the surface during the cutting. All the structures were cut close to the middle of the shape.

Nonlinear Optical Signal Measurements: Broadband PL and SHG signals' measurements were carried out under ultrafast laser pumping by the TEMA-150 fs laser with repetition rate of 80 MHz. Laser power was varied by attenuator in range of 5–20 mW. After going through attenuator, laser pulse was focused on the hybrid structures from the substrate side by an objective (M = 10×, NA = 0.26). The excited PL and SHG signals were collected by the VIS objective with M = 100× and NA = 0.70 from the top side of sample. Collected signal was sent to spectrometer Horiba Jobin-Yvon LabRam HR800 with diffraction grating 150 lines per mm while pumping signal was attenuated in 10^4 times by FESH850 filter, which was placed before spectrometer.

Statistical Analysis: All statistical analyses were done in Python language. The variation in reading a PUF label and label-to-label variation were counted from the nonlinear signal maps of six labels, all of which consisted of ten structures. The result is presented in Figure S4b, Supporting Information, as mean ± standard deviation for every point of final spectrum.

Supporting Information

Supporting Information is available from the Wiley Online Library or from the author.

Conflict of Interest

The authors declare no conflict of interest.

Data Availability Statement

Research data are not shared.

[1] T. Staake, F. Thiesse, E. Fleisch, *Eur. J. Mark.* **2009**, *43*, 320.

[2] A. K. Deisingh, *Analyst* **2005**, *130*, 271.

[3] World Health Organization, https://www.who.int/multi-media/details/substandard-and-falsified-medicines-kill-hundreds-of-thousands-of-people-globally, (accessed: June 2022).

[4] G. Khalil, R. Doss, M. Chowdhury, *J. Sens. Actuator Networks* **2019**, *8*, 37.

[5] R. Chen, Y. Yu, J. Chen, Y. Zhong, H. Zhao, A. Hussain, H.-Z. Tan, *Sensors* **2020**, *20*, 4926.

[6] G. Ruffato, R. Rossi, M. Massari, E. Mafakheri, P. Capaldo, F. Romanato, *Sci. Rep.* **2017**, *7*, 18011.

[7] T. Dekel, M. Rubinstein, C. Liu, W. T. Freeman, in *Proc. of the IEEE Conf. on Computer Vision and Pattern Recognition*, IEEE, Piscataway, NJ **2017**, pp. 2146–2154.

[8] M. Zuo, W. Qian, T. Li, X.-Y. Hu, J. Jiang, L. Wang, *ACS Appl. Mater. Interfaces* **2018**, *10*, 39214.

[9] R. Arppe, T. J. Sørensen, *Nat. Rev. Chem.* **2017**, *1*, 0031.

[10] J. D. Buchanan, R. P. Cowburn, A.-V. Jausovec, D. Petit, P. Seem, G. Xiong, D. Atkinson, K. Fenton, D. A. Allwood, M. T. Bryan, *Nature* **2005**, *436*, 475.

[11] R. Cowburn, *Contemp. Phys.* **2008**, *49*, 331.

[12] J. Kim, J. M. Yun, J. Jung, H. Song, J.-B. Kim, H. Ihee, *Nanotechnology* **2014**, *25*, 155303.

[13] Z. Hu, J. M. M. L. Comeras, H. Park, J. Tang, A. Afzali, G. S. Tulevski, J. B. Hannon, M. Liehr, S.-J. Han, *Nat. Nanotechnol.* **2016**, *11*, 559.

[14] A. F. Smith, P. Patton, S. E. Skrabalak, *Adv. Funct. Mater.* **2016**, *26*, 1315.

[15] O. Ivanova, A. Elliott, T. Campbell, C. Williams, *Addit. Manuf.* **2014**, *1*, 24.

[16] Y. Zheng, C. Jiang, S. H. Ng, Y. Lu, F. Han, U. Bach, J. J. Gooding, *Adv. Mater.* **2016**, *28*, 2330.

[17] Y. Liu, F. Han, F. Li, Y. Zhao, M. Chen, Z. Xu, X. Zheng, H. Hu, J. Yao, T. Guo, W. Lin, Y. Zheng, B. You, P. Liu, Y. Li, L. Qian, *Nat. Commun.* **2019**, *10*, 2409.

[18] L. Tian, K.-K. Liu, M. Fei, S. Tadepalli, S. Cao, J. A. Geldmeier, V. V. Tsukruk, S. Singamaneni, *ACS Appl. Mater. Interfaces* **2016**, *8*, 4031.

[19] H. J. Bae, S. Bae, C. Park, S. Han, J. Kim, L. N. Kim, K. Kim, S.-H. Song, W. Park, S. Kwon, *Adv. Mater.* **2015**, *27*, 2123.

[20] R. Pappu, B. Recht, J. Taylor, N. Gershenfeld, *Science* **2002**, *297*, 2026.

[21] J. D. Smith, M. A. Reza, N. L. Smith, J. Gu, M. Ibrar, D. J. Crandall, S. E. Skrabalak, *ACS Nano* **2021**, *15*, 2901.

[22] Y. Gu, C. He, Y. Zhang, L. Lin, B. D. Thackray, J. Ye, *Nat. Commun.* **2020**, *11*, 516.

[23] Y. Li, Z. Liu, K. Zhu, L. Ai, P. Jia, N. Wu, H. Yu, J. Wang, X. Yao, J. Zhou, Y. Song, *Adv. Mater. Interfaces* **2021**, *8*, 2101281.

[24] V. Caligiuri, A. Patra, M. P. De Santo, A. Forestiero, G. Papuzzo, D. M. Aceti, G. E. Lio, R. Barberi, A. De Luca, *ACS Appl. Mater. Interfaces* **2021**, *13*, 49172.

[25] N. Kayaci, R. Ozdemir, M. Kalay, N. B. Kiremitler, H. Usta, M. S. Onses, *Adv. Funct. Mater.* **2022**, *32*, 2108675.

[26] V. Kumar, S. Dottermusch, N. Katumo, A. Chauhan, B. S. Richards, I. A. Howard, *Adv. Opt. Mater.* **2022**, *10*, 2102402.

[27] M. R. Carro-Temboury, R. Arppe, T. Vosch, T. J. Sørensen, *Sci. Adv.* **2018**, *4*, e1701384.

[28] A. Abdollahi, H. Roghani-Mamaqani, B. Razavi, M. Salami-Kalajahi, *ACS Nano* **2020**, *14*, 14417.

[29] Z. Zeng, B. Huang, X. Wang, L. Lu, Q. Lu, M. Sun, T. Wu, T. Ma, J. Xu, Y. Xu, S. Wang, Y. Du, C.-H. Yan, *Adv. Mater.* **2020**, *32*, 2004506.

[30] X. Yu, H. Zhang, J. Yu, *Aggregate* **2021**, *2*, 20.

[31] N. Livakas, E. Skoulas, E. Stratakis, *Opto-Electron. Adv.* **2020**, *3*, 190035.

[32] Q. Yang, H. Liu, S. He, Q. Tian, B. Xu, P. Wu, *Opto-Electron. Adv.* **2021**, *4*, 200005.

[33] V. P. Veiko, Y. Andreeva, L. Van Cuong, D. Lutoshina, D. Polyakov, D. Sinev, V. Mikhailovskii, Y. R. Kolobov, G. Odintsova, *Optica* **2021**, *8*, 577.

[34] S. Cucerca, P. Didyk, H.-P. Seidel, V. Babaei, *ACM Trans. Graphics* **2020**, *39*, 70.

[35] A. Y. Zhizhchenko, P. Tonkaev, D. Gets, A. Larin, D. Zuev, S. Starikov, E. V. Pustovalov, A. M. Zakharenko, S. A. Kulinich, S. Juodkazis, A. A. Kuchmizhak, S. V. Makarov, *Small* **2020**, *16*, 2000410.

[36] S. Hayashi, K. Tsunemitsu, M. Terakawa, *Nano Lett.* **2021**, *22*, 775.

[37] A. O. Larin, L. N. Dvoretckaia, A. M. Mozharov, I. S. Mukhin, A. B. Cherepakhin, I. I. Shishkin, E. I. Ageev, D. A. Zuev, *Adv. Mater.* **2021**, *33*, 2005886.

[38] Z. Ma, J. Zhou, J. Zhang, S. Zeng, H. Zhou, A. T. Smith, W. Wang, L. Sun, Z. Wang, *Mater. Horiz.* **2019**, *6*, 2003.

[39] S. Kalytchuk, Y. Wang, K. Poláková, R. Zbořil, *ACS Appl. Mater. Interfaces* **2018**, *10*, 29902.

[40] J.-H. Wei, J.-F. Liao, L. Zhou, J.-B. Luo, X.-D. Wang, D.-B. Kuang, *Sci. Adv.* **2021**, *7*, eabg3989.

[41] Y. P. Meshcheryakov, N. Bulgakova, *Appl. Phys. A* **2006**, *82*, 363.

[42] A. Kuchmizhak, O. Vitrik, Y. Kulchin, D. Storozhenko, A. Mayor, A. Mirochnik, S. Makarov, V. Milichko, V. Kudryashov, V. Zhakhovsky, N. Inogamov, *Nanoscale* **2016**, *8*, 12352.

[43] S.-G. Ryu, I. Gruber, C. P. Grigoropoulos, D. Poulikakos, S.-J. Moon, *Thin Solid Films* **2012**, *520*, 6724.

[44] B. I. Afinogenov, A. N. Sofronov, I. M. Antropov, N. R. Filatov, A. S. Medvedev, A. S. Shorokhov, V. N. Mantsevich, N. S. Maslova, T. Kim, E. Jeang, I. Kim, M. Seo, K. Han, S. Bae, W. Joo, H. Yoo, V. O. Bessonov, A. A. Fedyanin, M. V. Ryabko, S. V. Polonsky, *Opt. Lett.* **2021**, *46*, 3071.

[45] C.-H. Cho, C. O. Aspetti, J. Park, R. Agarwal, *Nat. Photonics* **2013**, *7*, 285.

[46] J. Xiang, M. Panmai, S. Bai, Y. Ren, G.-C. Li, S. Li, J. Liu, J. Li, M. Zeng, J. She, Y. Xu, S. Lan, *Nano Lett.* **2021**, *21*, 2397.

[47] A. Larin, E. Ageev, D. Zuev, *AIP Conf. Proc.* **2020**, *2300*, 020078.

[48] T. Ehmke, A. Knebl, S. Reiss, I. R. Fischinger, T. G. Seiler, O. Stachs, A. Heisterkamp, *AIP Adv.* **2015**, *5*, 084903.

[49] A. V. Zayats, T. Kalkbrenner, V. Sandoghdar, J. Mlynek, *Phys. Rev. B* **2000**, *61*, 4545.

[50] S. V. Makarov, M. I. Petrov, U. Zywietz, V. Milichko, D. Zuev, N. Lopanitsyna, A. Kuksin, I. Mukhin, G. Zograf, E. Ubyivovk, D. A. Smirnova, S. Starikov, B. N. Chichkov, Y. S. Kivshar, *Nano Lett.* **2017**, *17*, 3047.

[51] J. Dai, J.-H. Zeng, S. Lan, X. Wan, S.-L. Tie, *Opt. Express* **2013**, *21*, 10025.

[52] S. Makarov, I. S. Sinev, V. A. Milichko, F. Komissarenko, D. Zuev, E. V. Ushakova, I. Mukhin, Y. F. Yu, A. I. Kuznetsov, P. Belov, I. V. Iorsh, A. N. Poddubny, A. K. Samusev, Y. S. Kivshar, *Nano Lett.* **2018**, *18*, 535.

[53] F. Chen, Q. Li, M. Li, F. Huang, H. Zhang, J. Kang, P. Wang, *Chem. Eng. J.* **2021**, *411*, 128350.

[54] H. Im, J. Yoon, J. Choi, J. Kim, S. Baek, D. H. Park, W. Park, S. Kim, *Adv. Mater.* **2021**, *33*, 2102542.

[55] Y. Liu, Y. Zheng, Y. Zhu, F. Ma, X. Zheng, K. Yang, X. Zheng, Z. Xu, S. Ju, Y. Zheng, T. Guo, L. Qian, F. Li, *ACS Appl. Mater. Interfaces* **2020**, *12*, 39649.

[56] Y.-W. Hu, T.-P. Zhang, C.-F. Wang, K.-K. Liu, Y. Sun, L. Li, C.-F. Lv, Y.-C. Liang, F.-H. Jiao, W.-B. Zhao, L. Dong, C.-X. Shan, *Adv. Funct. Mater.* **2021**, *31*, 2102108.

[57] O. Günlü, P. Trifonov, M. Kim, R. F. Schaefer, V. Sidorenko, in *2020 Int. Symp. on Information Theory and Its Applications (ISITA)*, IEEE, Piscataway, NJ **2020**, pp. 475–479.

[58] H. Imai, S. Hirakawa, *IEEE Trans. Inf. Theory* **1977**, *23*, 371.

[59] S. Puchinger, S. Muelich, M. Bossert, M. Hiller, G. Sigl, in *Proc. of Int. ITG Conf. on Systems, Communications and Coding*, VDE VERLAG, Berlin, Germany **2015**, pp. 1–6.

[60] B. Chen, T. Ignatenko, F. M. J. Willems, R. Maes, E. van der Sluis, G. Selimis, in *Proc. of IEEE Global Communications Conf.*, IEEE, Piscataway, NJ **2017**, pp. 1–6.

[61] O. Gunlu, O. Iscan, V. R. Sidorenko, G. Kramer, *IEEE Trans. Inf. Forensics Secur.* **2019**, *14*, 11.